# Spin Crossover in Ferropericlase at High Pressure: A Seismologically Transparent Transition?

Daniele Antonangeli, *et al.*

*Science* **331**, 64 (2011);
DOI: 10.1126/science.1198429

3C) quantitatively reproduce the main features discussed above. Inspection of the trajectories responsible for the side-lobes shows that these trajectories can indeed be considered as a reference and scattered wave packet, creating a hologram (Fig. 4A).

The efficiency of electron-ion recollision drops dramatically with increasing $\lambda_{laser}$ because of spreading of the wave packet between ionization and recollision. Still, a clear hologram can be observed at 7 μm. Two effects make this possible. First, the hologram results from a heterodyne experiment, in which a weaker signal is mixed with a stronger signal. Second, to create a clear reference a large-impact parameter is needed in order to limit the interaction with the Coulomb field. For large $\lambda_{laser}$, a small $p_r$ already leads to large-impact parameters because of the long excursion time between ionization and recollision.

Inspection of the electron trajectories contributing to the transverse structures (Fig. 3) reveals that they are due to recollision events in which the scattering does not occur on the first opportunity but on the second or third (*20*, *24*, *25*). Typical examples of these trajectories are shown in Fig. 4, B to D. One, respectively two glancing electron-ion collisions can be observed before the real recollision takes place. Usually, these rare events do not leave an imprint on the photoelectron spectrum. However, the combination of a long laser wavelength and Coulomb focusing (*24*) increases the probability because a small deviation introduced by the Coulomb potential can be sufficient to focus the returning wave packet onto the ion.

In our model study on the ionization of metastable xenon, we have experimentally shown the possibility to record holographic structures. Furthermore, our theoretical exploration shows that the hologram stores spatial and temporal information about the core- and electron dynamics. This offers opportunities to extend strong-field holography to more complicated systems and to use it to time-resolve electron-dynamics. As revealed in recent experiments (*6*, *26*), electron-ion recollision phenomena encode hole dynamics that occur in ions during the first few femtoseconds after strong-field ionization. When properly implemented with the use of a long-wavelength-driving laser, photo-electron holography appears especially well suited for studying this type of dynamics, in particular in molecules with a low binding energy that cannot easily be studied by other means.

### References and Notes


1. P. B. Corkum, *Phys. Rev. Lett.* **71**, 1994 (1993).
2. F. Krausz, M. Y. Ivanov, *Rev. Mod. Phys.* **81**, 163 (2009).
3. M. F. Kling, M. J. J. Vrakking, *Annu. Rev. Phys. Chem.* **59**, 463 (2008).
4. J. Itatani *et al.*, *Nature* **432**, 867 (2004).
5. D. Shafir, Y. Mairesse, D. M. Villeneuve, P. B. Corkum, N. Dudovich, *Nat. Phys.* **5**, 412 (2009).
6. O. Smirnova *et al.*, *Nature* **460**, 972 (2009).
7. S. Baker *et al.*, *Science* **312**, 424 (2006).
8. M. Meckel *et al.*, *Science* **320**, 1478 (2008).
9. M. Spanner, O. Smirnova, P. B. Corkum, M. Y. Ivanov, *J. Phys. At. Mol. Opt. Phys.* **37**, L243 (2004).
10. H. Niikura *et al.*, *Nature* **417**, 917 (2002).
11. D. Gabor, *Nobel Lectures, Physics 1971-1980* (World Scientific, Singapore, 1992).
12. G. G. Paulus *et al.*, *Phys. Rev. Lett.* **84**, 3791 (2000).
13. J. Mauritsson *et al.*, *Phys. Rev. Lett.* **100**, 073003 (2008).
14. Materials and methods are available as supporting material on *Science* Online.
15. W. Becker, A. Lohr, M. Kleber, *J. Phys. At. Mol. Opt. Phys.* **27**, L325 (1994).
16. M. Lewenstein, K. C. Kulander, K. J. Schafer, P. H. Bucksbaum, *Phys. Rev. A* **51**, 1495 (1995).
17. J. M. Bakker *et al.*, *J. Chem. Phys.* **132**, 074305 (2010).
18. A. T. J. B. Eppink, D. H. Parker, *Rev. Sci. Instrum.* **68**, 3477 (1997).
19. B. R. Yang *et al.*, *Phys. Rev. Lett.* **71**, 3770 (1993).
20. G. G. Paulus, W. Becker, W. Nicklich, H. Walther, *J. Phys. At. Mol. Opt. Phys.* **27**, L703 (1994).
21. R. Gopal *et al.*, *Phys. Rev. Lett.* **103**, 053001 (2009).
22. H. G. Muller, *Laser Phys.* **9**, 138 (1999).
23. S. V. Popruzhenko, D. Bauer, *J. Mod. Opt.* **55**, 2573 (2008).
24. T. Brabec, M. Y. Ivanov, P. B. Corkum, *Phys. Rev. A* **54**, R2551 (1996).
25. G. L. Yudin, M. Y. Ivanov, *Phys. Rev. A* **63**, 033404 (2001).
26. Y. Mairesse *et al.*, *Phys. Rev. Lett.* **104**, 213601 (2010).


27. We acknowledge R. Kemper, H. Schoenmaker, A. de Snaijer, I. Cerjak, and the staff at the FELIX facility for their great technical assistance. This work is part of the research program of FOM, which is financially supported by the Nederlandse organisatie voor Wetenschappelijk Onderzoek (NWO). K.J.S. is supported by NSF grant PHY-0701372 and the Ball Professorship at LSU. M.Y.I. is supported by Science and Innovation grant EP/E036112/1 of the Engineering and Physical Sciences Research Council. O.S. acknowledges a Leibniz SAW award.


### Supporting Online Material

www.sciencemag.org/cgi/content/full/science.1198450/DC1
Materials and Methods
SOM Text
Figs. S1 to S5
References

29 September 2010; accepted 7 December 2010
Published online 6 December 2010;
10.1126/science.1198450

# Spin Crossover in Ferropericlase at High Pressure: A Seismologically Transparent Transition?

**Daniele Antonangeli,[1,2]* Julien Siebert,[1,2] Chantel M. Aracne,[2] Daniel L. Farber,[2,3] A. Bosak,[4] M. Hoesch,[4] M. Krisch,[4] Frederick J. Ryerson,[2] Guillaume Fiquet,[1] James Badro[1,2]**

**Seismic discontinuities in Earth typically arise from structural, chemical, or temperature variations with increasing depth. The pressure-induced iron spin state transition in the lower mantle may influence seismic wave velocities by changing the elasticity of iron-bearing minerals, but no seismological evidence of an anomaly exists. Inelastic x-ray scattering measurements on $(Mg_{0.83}Fe_{0.17})O$-ferropericlase at pressures across the spin transition show effects limited to the only shear moduli of the elastic tensor. This explains the absence of deviation in the aggregate seismic velocities and, thus, the lack of a one-dimensional seismic signature of the spin crossover. The spin state transition does, however, influence shear anisotropy of ferropericlase and should contribute to the seismic shear wave anisotropy of the lower mantle.**

The characterization of pressure- and temperature-induced transformations in mantle minerals and their connection to seismic discontinuities aid in the understanding of Earth's interior. In this sense, the series of phase transformations that occurs in olivine—which with increasing pressure first transforms to wadsleyite, then to ringwoodite, and then breaks down into ferropericlase and perovskite—is emblematic. These phase changes are accompanied by density and sound-velocity variations that are responsible for the main seismic discontinuities in the upper mantle (*1*).

In contrast, the recently discovered iron spin-state transition—where compression favors the electron spin pairing, with the system changing from a high-spin to a low-spin state—in both ferropericlase (*2*) and perovskite (*3*), the two main phases of the lower mantle, does not clearly relate to any seismic signature, although effects on mantle density and seismic wave velocity have been anticipated (*4*–*8*). In ferropericlase, the spin transition occurs without structural changes (*4*, *9*), but experimental (*10*) and theoretical (*11*) studies suggest large softening of all the elastic moduli and, consequently, a major decrease in the aggregate sound velocities. Thus, at pressure and temperature conditions of the lower mantle, such an effect should be associated to a broad seismic anomaly (*12*) that, conversely, is not observed (*13*, *14*).

Here we present inelastic x-ray scattering (IXS) measurements on $(Mg_{0.83}Fe_{0.17})O$-ferropericlase across the spin transition and up to 70 GPa (*15*). We obtained the complete elastic tensor (that is,

[1]Institut de Minéralogie et de Physique des Milieux Condensés, UMR CNRS 7590, Institut de Physique du Globe de Paris, Université Pierre et Marie Curie, Université Paris Diderot, 75005 Paris, France. [2]Lawrence Livermore National Laboratory, Livermore, CA 94550, USA. [3]Department of Earth and Planetary Sciences, University of California, Santa Cruz, Santa Cruz, CA, 95064, USA. [4]European Synchrotron Radiation Facility, BP 220, 38043 Grenoble Cedex, France.

*To whom correspondence should be addressed. E-mail: daniele.antonangeli@impmc.upmc.fr

all of the independent moduli that linearly relate stress and strain) and derived the aggregate sound velocities, the aggregate elastic moduli, and the shear anisotropy at corresponding depth. IXS has proven to be a useful technique for the high-pressure and high-temperature study of elasticity and sound velocities of powders (*16*–*18*) and single crystals (*19*, *20*). In particular, IXS allows all of the independent elements of the elastic tensor to be directly determined from the initial slope of the phonon dispersion of selected longitudinal acoustic (LA) and transverse acoustic (TA) modes, without any external input or a priori model (*15*). Thus, IXS overcomes the limitations of previously used surface-sensitive techniques [such as impulsive stimulated light scattering (ISLS) (*8*, *21*)] that require a complex data inversion, involving modeling of the sound waves at the interfaces and input of external parameters to obtain bulk properties. Brillouin measurements, which also directly provide sound velocities, were limited in the case of ferropericlase to the only shear velocities and the longitudinal moduli computed after input of the (independently measured) bulk modulus (*22*). IXS allows for the in situ determination of sample density (*15*), which is an important parameter in the mixed-spin region. Furthermore, whereas Brillouin scattering is restricted to transparent samples (*22*–*24*), IXS is not. Thus, we have been able to investigate high–iron-content ferropericlase [17 mole percent (mol %) Fe], which is more relevant to the lower mantle than that used in recent work (*8*, *22*–*24*).

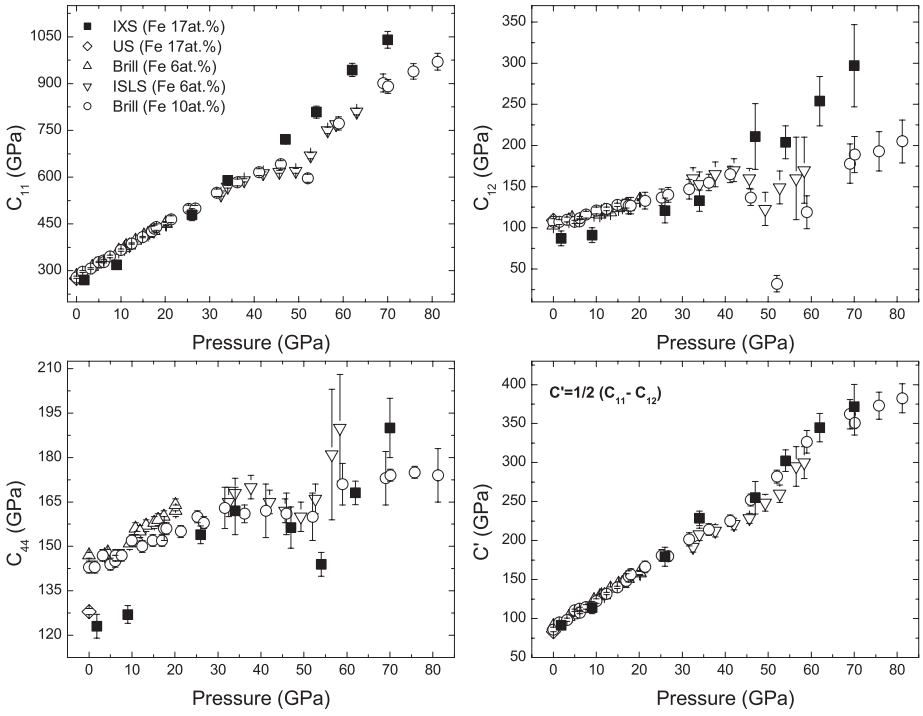


**Fig. 1.** Pressure evolution of the single-crystal elastic moduli of $(Mg_{1-x},Fe_x)O$-ferropericlase (table S1) (*15*). Solid squares, IXS data for $x = 0.17$ (this work); open diamonds, ambient pressure ultrasonic determinations for $x = 0.17$ (*26*); open triangles, Brillouin measurements for $x = 0.06$ (*23*); open inverted triangles, ISLS results for $x = 0.06$ (*10*); open circles, Brillouin determinations for $x = 0.10$ (*22*). Error bars account for the uncertainties on the measured velocities and densities (*15*). at. %, atomic percent.

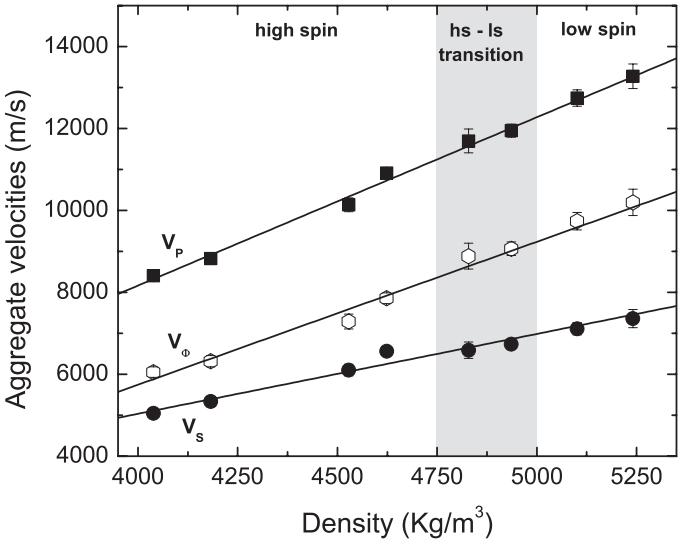


**Fig. 2.** Density evolution of the aggregate sound velocities (Voigt-Reuss-Hill average) (*15*). Solid squares, compressional sound velocity ($V_P$); solid circles, shear sound velocity ($V_S$); open hexagons, bulk sound velocity ($V_\Phi = \sqrt{K/\rho}$). The lines are linear fits to the experimental data. The density range corresponding to the spin-transition zone (4750 to 5000 kg/m$^3$) is shaded. Error bars on the aggregate velocities come from the propagation of the uncertainties on the elastic moduli and the difference between the Voigt and Reuss average (*15*).

Up to ~40 GPa, all the elastic moduli exhibit a monotonic increase with pressure (Fig. 1 and table S1), as is expected with compression. In the 40–to–60-GPa pressure range, where the spin transition occurs (*2*, *4*, *25*), we observe a distinct softening of $C_{44}$ and a small variation in $C_{12}$, whereas $C_{11}$ retains a continuous trend. Above 60 GPa, the usual monotonic increase with pressure is observed for all of the moduli, albeit with a larger pressure derivative. The back extrapolations of our results to ambient pressure are within a few percent of the ultrasonic determinations for the same composition (*26*). However, if we compare our high-pressure measurements with ISLS (*10*) and Brillouin (*22*, *24*) data obtained on samples with lower iron content, we observe qualitative agreement for $C_{44}$ and $C' = 1/2(C_{11} - C_{12})$, which display softening in the pressure range of the spin transition for all methods (quantitative differences are at least partially due to differences in iron concentration), but disagreement for $C_{12}$ and $C_{11}$. Whereas both optical studies (*8*, *22*) report a large softening of $C_{11}$ in the 40–to–60-GPa range, the direct determination of $C_{11}$ by IXS [via sound velocity measurements of the LA[100] mode (*15*)] does not show any anomaly (Fig. 1). To support our findings, we stress that in other systems where pressure-induced, spin-pairing transitions occur (such as the extensively investigated Fe-, Co-, and Mn-Invar alloys), these transitions are commonly accompanied by much larger effects on the shear elastic moduli than on the longitudinal moduli (*27*, *28*).

From the measured single-crystalline $C_{ij}$, we computed the aggregate elastic properties bulk and shear moduli, as well as the compressional ($V_P$) and shear ($V_S$) sound velocities by straightforward averaging [see (*15*)]. The values we obtain for the bulk and shear moduli compare favorably with the ambient-pressure ultrasonic determination (*26*) and with the values obtained by x-ray diffraction (*4*) for both the low-spin and the high-spin state (figs. S3 and S4).

A direct consequence of the lack of softening of $C_{11}$ and of the moderate effect on $C_{12}$ is the absence of any sizable deviation from a linear density evolution of the aggregate $V_P$ and $V_S$ (Fig. 2). In contrast to recent claims (*8*, *11*, *22*),

neither $V_P$ nor $V_S$ show an anomaly due to the spin-pairing transition.

With respect to Earth's lower mantle, recent optical (*8*, *22*) and theoretical (*11*) studies proposed that an anomalous (albeit smooth) softening of the aggregate elastic properties (especially the bulk modulus $K$ and the bulk velocity $V_\Phi = \sqrt{K/\rho}$, where ρ is density) should occur at depth. The range over which this takes place has been suggested to extend from 1000 to 1500 km, based on room-temperature results (*8*), and from 1300 to 1800 km, when including high-temperature effects (*22*), such as those along a mantle geotherm (*11*). Our study provides an explanation for the lack of a seismic signature (*13*, *14*) associated with the spin crossover in the lower mantle.

The high-spin–to–low-spin transition does, however, have an effect on the single-crystal elasticity of ferropericlase (when not smeared due to averaging over many grains as in an ideally random aggregate). The relative magnitude of the shear elastic moduli $C_{44}$ and $C'$ (corresponding to the sound velocity of the $TA[110]_{<001>}$ and $TA[110]_{<-110>}$ modes, respectively) evolves with pressure (Fig. 3). At ambient and low pressures, $C_{44} > C'$, but the pressure derivative of $C'$ is larger than that of $C_{44}$, so that the two intersect around 16 to 17 GPa. At higher pressures, the sign of shear anisotropy is reversed. This behavior is in good agreement with results of Brillouin spectroscopy on samples with 10 mol % Fe (*24*). Above 60 GPa, in the low-spin phase, the pressure derivative of the two shear moduli is almost the same. Accordingly, the pressure evolution of the shear anisotropy, defined as $A = 2(C' - C_{44})/(C' + C_{44})$, is very different for the high- and low-spin ferropericlase (see inset of Fig. 3): $A$ increases linearly with pressure in the high-spin phase, whereas it remains almost constant (or slightly decreases) in the low-spin phase. Thus, we suggest that a seismically detectable signature of the spin transition in the lower mantle may be found in the shear anisotropy. Because ferropericlase is much weaker than perovskite, it can accommodate most of the strain (*29*) and develop strong texture (*30*). Our measurements indicate a very large shear anisotropy, ~70% at 70 GPa for ferropericlase with a Fe content of 17 mol %, a value very close to that measured for ferropericlase with 10 mol % Fe (*24*) and at least 50% larger than the shear anisotropy of MgO (*24*). Such a considerable anisotropy, in conjunction with lattice-preferred orientation, supports the notion that ferropericlase is the main phase responsible for the seismic shear anisotropy of the lower mantle (*24*). Therefore, the different shear anisotropy behavior of high- and low-spin ferropericlase should be considered together with temperature and chemical variations to interpret local seismic heterogeneity.

Finally, the values of $V_P$ and $V_S$ for $(Mg_{0.83}Fe_{0.17})O$-ferropericlase at 70 GPa (13300 ± 300 m/s and 7360 ± 220 m/s, respectively) are very close to the measured $V_S$ (*31*) and computed $V_P$ and $V_S$ (*32*, *33*) values for $MgSiO_3$-perovskite at the same pressure. Because both Fe and Al are expected to lower the aggregate velocities of perovskite (*33*, *34*), our results suggest that the velocities of the two major phases of the lower mantle might become comparable (if not ferropericlase faster than perovskite) in the lowermost 1000 to 1200 km of the lower mantle. This could challenge current compositional models of the lowermost mantle based on an extrapolation of lower-pressure elasticity data. However, direct high-pressure, high-temperature measurements on both ferropericlase and perovskite (with relevant major-element compositions) are required to confirm these conjectures.

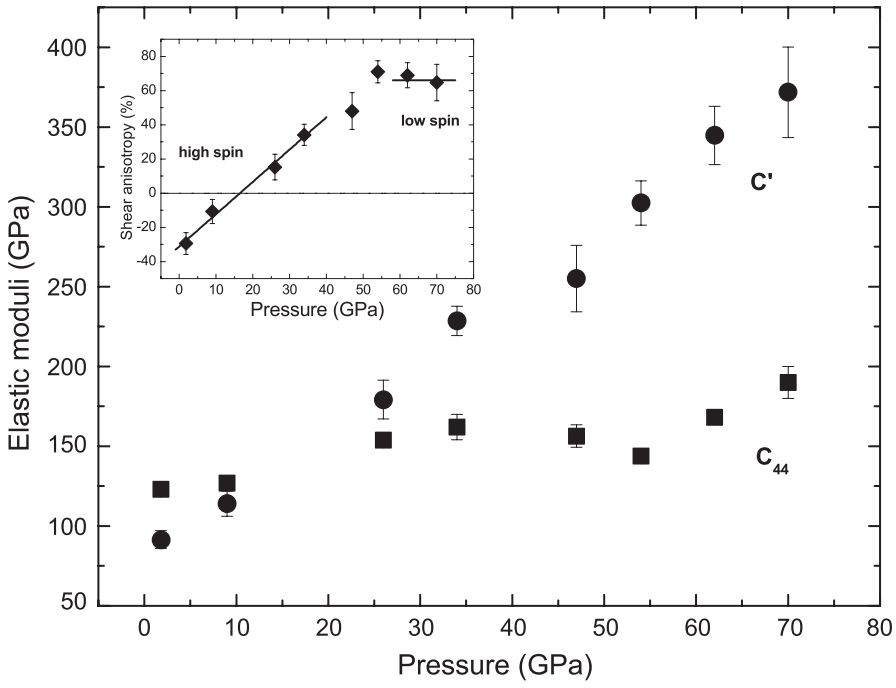


**Fig. 3.** Comparison of the pressure evolution of $C_{44}$ (squares) and $C'$ (circles), corresponding to the two different polarizations of the shear mode in the diagonal plane of a cubic lattice. (**Inset**) Shear anisotropy as a function of pressure. The lines are guides for the eye. Error bars account for the uncertainties on the measured velocities and densities (*15*).

**References and Notes**


1. J.-P. Poirier, *Introduction to the Physics of the Earth's Interior* (Cambridge Univ. Press, Cambridge, 2000).
2. J. Badro *et al.*, *Science* **300**, 789 (2003); 10.1126/science.1081311.
3. J. Badro *et al.*, *Science* **305**, 383 (2004).
4. J.-F. Lin *et al.*, *Nature* **436**, 377 (2005).
5. J.-F. Lin *et al.*, *Geophys. Res. Lett.* **33**, L22304 (2006).
6. J.-F. Lin *et al.*, *Geophys. Res. Lett.* **34**, L09301 (2007).
7. S. Speziale *et al.*, *J. Geophys. Res.* **112**, B10212 (2007).
8. K. Catalli *et al.*, *Earth Planet. Sci. Lett.* **289**, 68 (2010).
9. Y. Fei *et al.*, *Geophys. Res. Lett.* **34**, L17307 (2007).
10. J. C. Crowhurst, J. M. Brown, A. F. Goncharov, S. D. Jacobsen, *Science* **319**, 451 (2008).
11. R. M. Wentzcovitch *et al.*, *Proc. Natl. Acad. Sci. U.S.A.* **106**, 8447 (2009).
12. J.-F. Lin *et al.*, *Science* **317**, 1740 (2007).
13. G. Masters, *Eos Trans. AGU* **89** (53), Fall Meet. Suppl., abstr. MR23A-04 (2008).
14. F. Cammarano, H. Marquardt, S. Speziale, P. J. Tackley, *Geophys. Res. Lett.* **37**, L03308 (2010).
15. Materials and methods are available as supporting material on *Science* Online.
16. D. Antonangeli *et al.*, *Earth Planet. Sci. Lett.* **225**, 243 (2004).
17. D. Antonangeli *et al.*, *Phys. Rev. B* **72**, 134303 (2005).
18. D. Antonangeli *et al.*, *Earth Planet. Sci. Lett.* **295**, 292 (2010).
19. D. Antonangeli *et al.*, *Phys. Rev. Lett.* **93**, 215505 (2004).
20. D. Antonangeli, M. Krisch, D. L. Farber, D. G. Ruddle, G. Fiquet, *Phys. Rev. Lett.* **100**, 085501 (2008).
21. J. C. Crowhurst *et al.*, *Appl. Phys. Lett.* **89**, 111920 (2006).
22. H. Marquardt, S. Speziale, H. J. Reichmann, D. J. Frost, F. R. Schilling, *Earth Planet. Sci. Lett.* **287**, 345 (2009).
23. J. M. Jackson *et al.*, *J. Geophys. Res.* **111**, B09203 (2006).
24. H. Marquardt *et al.*, *Science* **324**, 224 (2009).
25. A. F. Goncharov, V. V. Struzhkin, S. D. Jacobsen, *Science* **312**, 1205 (2006).
26. S. D. Jacobsen *et al.*, *J. Geophys. Res.* **107**, 2037 (2002).
27. F. Decremps, L. Nataf, *Phys. Rev. Lett.* **92**, 157204 (2004).
28. L. Nataf, F. Decremps, M. Gauthier, G. Syfosse, *Ultrasonics* **44** (suppl. 1), e555 (2006).
29. K. Madi, S. Forest, P. Cordier, M. Boussuge, *Earth Planet. Sci. Lett.* **237**, 223 (2005).
30. C. E. Tommaseo, J. Devine, S. Merkel, S. Speziale, H. K. Wenk, *Phys. Chem. Miner.* **33**, 84 (2006).
31. M. Murakami, S. Sinogeikin, H. Hellwig, J. Bass, J. Li, *Earth Planet. Sci. Lett.* **256**, 47 (2007).
32. A. R. Oganov, J. P. Brodholt, G. D. Price, *Earth Planet. Sci. Lett.* **184**, 555 (2001).
33. B. Kiefer, L. Stixrude, R. M. Wentzcovitch, *Geophys. Res. Lett.* **29**, 1539 (2002).

34. J. M. Jackson, J. Zhang, J. Shu, S. V. Sinogeikin, J. D. Bass, *Geophys. Res. Lett.* **32**, L21305 (2005).

35. We thank F. Occelli, G. Le Marchand, P. Munsch, P. Bouvier, M. Hanfland, M. Mezouar, and A. L. Auzende for experimental help. This work was performed under the auspices of the U.S. Department of Energy and Lawrence Livermore National Laboratory under contract DE-AC52-07NA27344 and was supported by the Office of Basic Energy Sciences–Geosciences Research Program (F.J.R.). D.A., J.B., and J.S. acknowledge financial support from the European Research Council (ERC) under the European Community's Seventh Framework Programme (FP7/2007-2013)/ERC grant agreement no. 207467. This work was supported by the French National Research Agency grant no. ANR-07-BLAN-0124-01 and ERC grant agreement no. 207467.

**Supporting Online Material**
www.sciencemag.org/cgi/content/full/331/6013/64/DC1
Materials and Methods
Figs. S1 to S4
Table S1
References and Notes

28 September 2010; accepted 6 December 2010
10.1126/science.1198429

# Small Interannual Variability of Global Atmospheric Hydroxyl

S. A. Montzka,[1]* M. Krol,[2,3] E. Dlugokencky,[1] B. Hall,[1] P. Jöckel,[4]† J. Lelieveld[4,5]

The oxidizing capacity of the global atmosphere is largely determined by hydroxyl (OH) radicals and is diagnosed by analyzing methyl chloroform ($CH_3CCl_3$) measurements. Previously, large year-to-year changes in global mean OH concentrations have been inferred from such measurements, suggesting that the atmospheric oxidizing capacity is sensitive to perturbations by widespread air pollution and natural influences. We show how the interannual variability in OH has been more precisely estimated from $CH_3CCl_3$ measurements since 1998, when atmospheric gradients of $CH_3CCl_3$ had diminished as a result of the Montreal Protocol. We infer a small interannual OH variability as a result, indicating that global OH is generally well buffered against perturbations. This small variability is consistent with measurements of methane and other trace gases oxidized primarily by OH, as well as global photochemical model calculations.

The hydroxyl radical (OH) is the primary oxidant for many non-$CO_2$ greenhouse gases, several stratospheric ozone-depleting substances and their substitutes, and hazardous air pollutants. It is also central to atmospheric photochemistry and the regulation of tropospheric ozone, and thus controls the influence of chemically reduced trace gases on climate, the stratospheric ozone layer, and air quality (*1*–*4*). The interannual variability (IAV) in OH concentrations ([OH]) on large spatial scales provides insight into the stability of the atmospheric oxidation capacity and its sensitivity to human-induced and natural perturbations. However, a consistent, predictive understanding of the net response of [OH] on broad scales to such perturbations is lacking. For example, a range of negative [OH] feedbacks is calculated from changes in atmospheric methane abundance (*3*, *5*–*7*).

Theory suggests that the sensitivity of [OH] to environmental changes depends on the relative importance of primary and secondary (recycling) OH formation pathways (*7*). The balance between primary OH formation initiated by ultraviolet light and formation by recycling is determined by atmospheric abundances and distributions of $NO_x$, $H_2O$, $O_3$, CO, and $CH_4$, as well as other parameters (*3*, *8*), many of which are highly variable in space and time and are relatively poorly characterized on global scales and in model calculations. As a result, calculated sensitivities of global [OH] to IAV in the chemical and physical makeup of the atmosphere have yet to be adequately tested.

Although OH can be measured directly on local scales, these results cannot characterize the integrated response of global mean [OH] to the many processes that control its formation and loss. Instead, indirect techniques are used in which [OH] is derived from observations of OH-oxidized trace gases such as $CH_3CCl_3$ and $^{14}CO$ (*9*–*19*). However, these approaches can suggest a very different sensitivity of [OH] to variations in the atmospheric environment than is derived in atmospheric models (*20*). Year-to-year changes in global [OH] as high as 20 to 25% have been derived from analyses of $CH_3CCl_3$ observations between 1980 and 2003, and these analyses imply a mean IAV of 7 to 9% (*16*, *17*). Chemistry transport models calculate a global [OH] variability of only 1 to 2%, but these models do not currently include variability in all factors influencing [OH] (*20*–*23*). Variations in [OH] of up to 20% have been estimated from $^{14}CO$, although only over a few months and on semihemispheric spatial scales (*19*).

Global mean [OH] can be estimated from atmospheric observations of a trace gas whose predominant sink is reaction with OH from mass balance considerations by equating the rate of change in the global burden ($dG/dt$) to the difference between the global emission rate ($E$) and loss. Solving for the pseudo–first-order rate constant for loss ($k_G$), which is proportional to [OH], gives

$$[\mathrm{OH}] \propto k_G = \frac{E}{G} - \frac{dG/dt}{G} \qquad (1)$$

where $G$ is the global burden estimated from surface measurements. Although $CH_3CCl_3$ losses (and $k_G$) are dominated by OH oxidation according to $k(T) \times [\mathrm{OH}]$, they include stratospheric photolysis, hydrolysis in surface waters, and other processes. Global mean [OH] derived in this

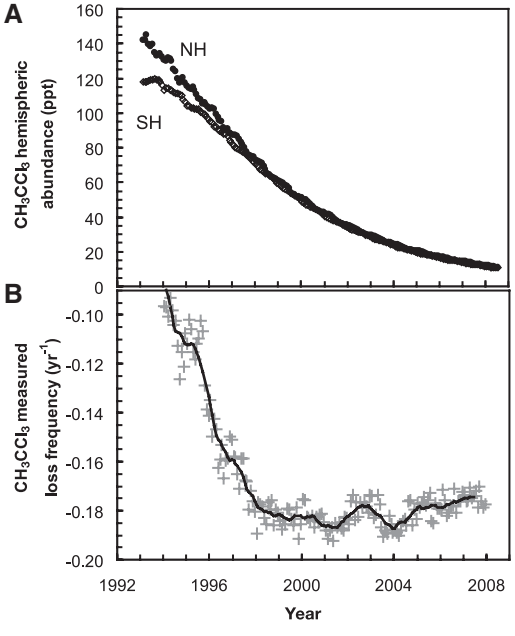


**Fig. 1.** (**A**) Observed hemispheric monthly mean mixing ratios of $CH_3CCl_3$ [update of (*14*)]. NH and SH denote Northern and Southern Hemispheres, respectively. (**B**) Exponential loss frequencies for $CH_3CCl_3$ derived from global surface means. Gray points are independent estimates derived from monthly means 12 months apart [e.g., $\ln(G_{\mathrm{Jan.\ 2007}}/G_{\mathrm{Jan.\ 2006}})$] plotted at the midpoint of this interval; the black line is the 12-month running mean.

[1]NOAA Earth System Research Laboratory, Boulder, CO 80305, USA. [2]Institute for Marine and Atmospheric Research Utrecht, University of Utrecht, 3584 CC Utrecht, Netherlands. [3]Meteorology and Air Quality Group, Wageningen University, 6708 PB Wageningen, Netherlands. [4]Department of Atmospheric Chemistry, Max Planck Institute for Chemistry, D-55128 Mainz, Germany. [5]Cyprus Institute, Nicosia 1645, Cyprus.

*To whom correspondence should be addressed. E-mail: stephen.a.montzka@noaa.gov
†Present address: Deutsches Zentrum für Luft- und Raumfahrt, Institut für Physik der Atmosphäre, Oberpfaffenhofen, D-82234 Wessling, Germany.